

Supplementary Material

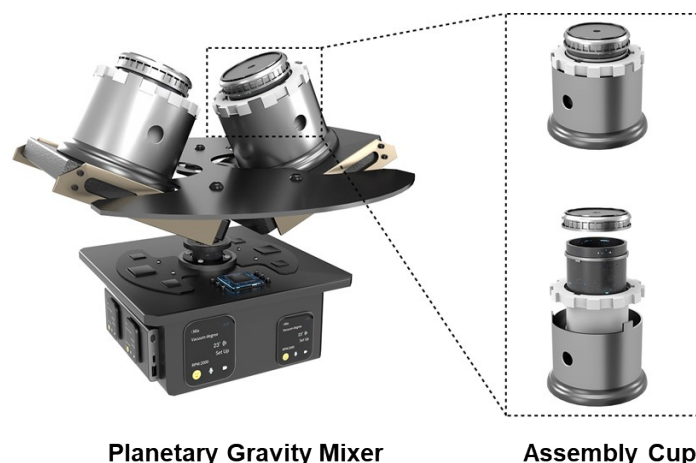
A hierarchical thermal interface material based on double self-assembly technique enables efficient output power via solar thermoelectric conversion

Yueyang Gao,^a Minghang Zhang,^a Yexiang Cui,^a Di Bao^b, Fei Xu,^a Xiaosong Shen,^a Yanji Zhu,^c and Huaiyuan Wang^{a*}

^aState Key Laboratory of Chemical Engineering, Department of Chemical Engineering and Technology, Tianjin University, Tianjin 300350, China. E-mail: huaiyuanwang@tju.edu.cn

^bCollege of Chemistry and Chemical Engineering, Northeast Petroleum University, Daqing 163318, China.

^cTianjin Key Lab Composite & Functional Materials, Department of Materials Science and Engineering, Tianjin University, Tianjin 300072, China.



Planetary Gravity Mixer

Assembly Cup

Figure S1. Schematic illustration of the planetary gravity mixer for the gravity-assisted assembly process.

Figure S1 exhibits the illustration of the planetary gravity mixer used for the gravity-assisted assembly process. The whole operation condition including the onset of the vacuum system and the stage mixing. The stage mixing often includes 3-4 phases with different rotation rates to fully complete the assembly and degassing procedure through gravity rotation.

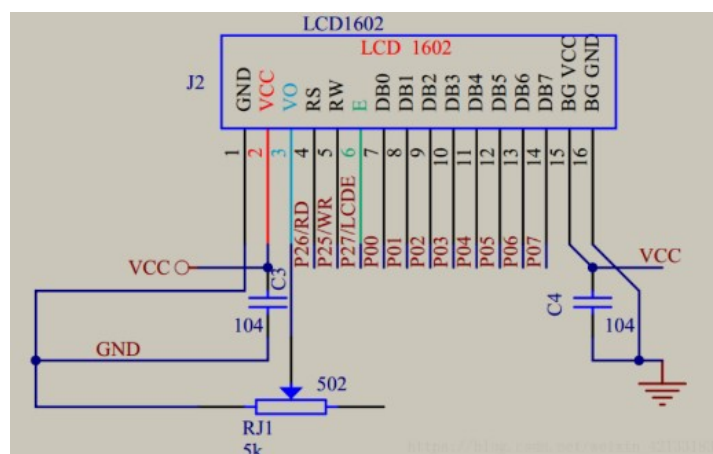


Figure S2. The circuit diagram of the LCD 1602 module.

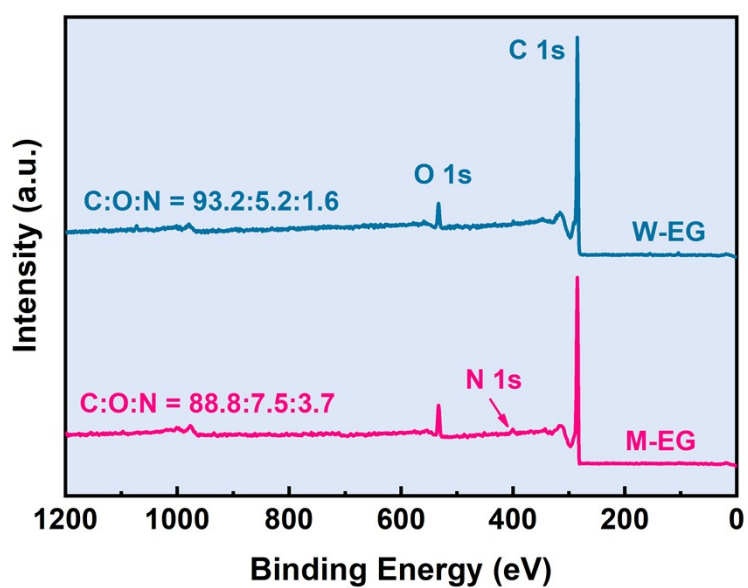


Figure S3. Full-range XPS spectra of the W-EG and M-EG sheets.

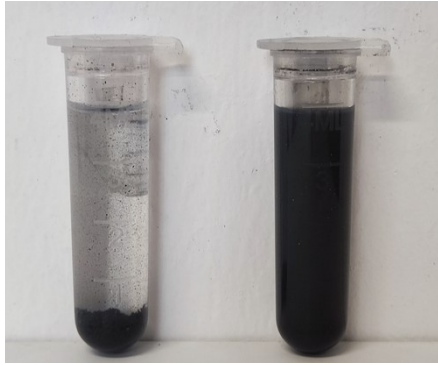


Figure S4. Dispersity of W-EG and M-EG in the deionized water.

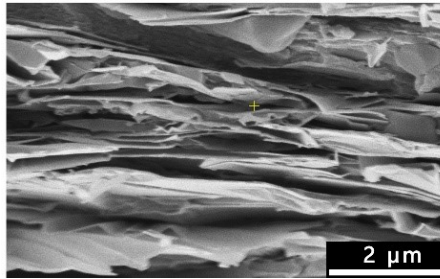


Figure S5. SEM image of the M-EG/Gel-Am composite with the extended vacuum assembly process.

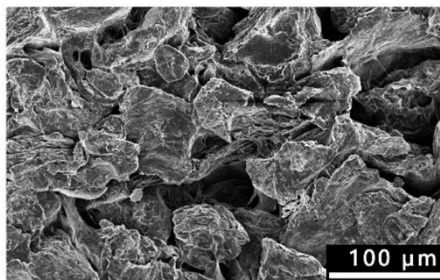


Figure S6. SEM image of the composite prepared by the direct consolidation without the vacuum-assisted procedure.

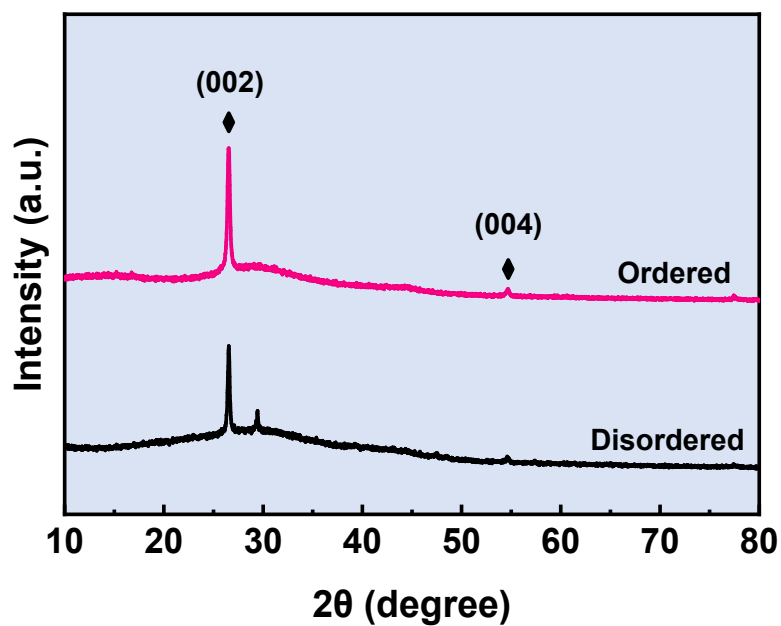


Figure S7. XRD results of the composite with ordered microstructure.

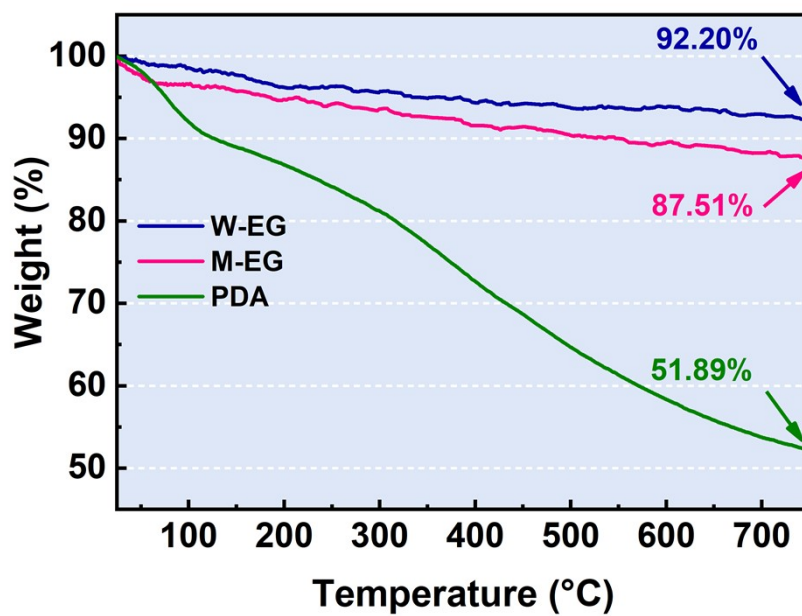


Figure S8. TGA curves of W-EG, M-EG, and PDA.

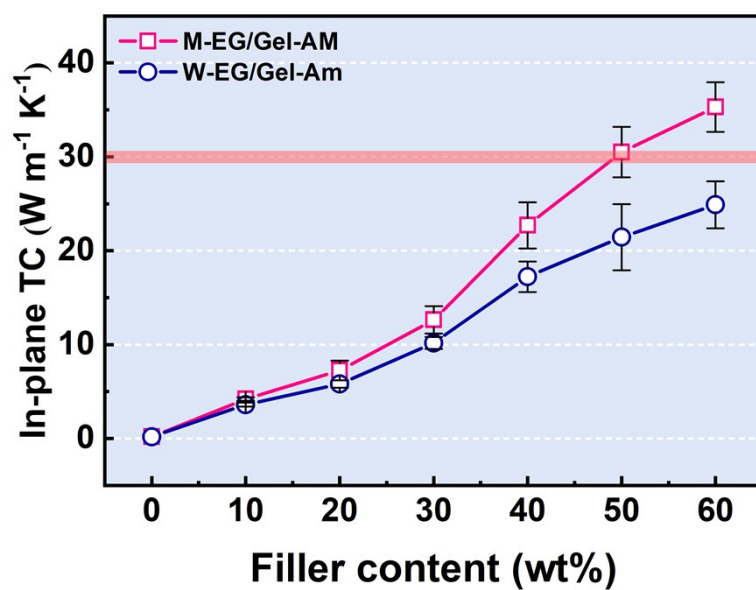


Figure S9. In-plane TC of W-EG/Gel-Am and M-EG/Gel-Am at different filler content.

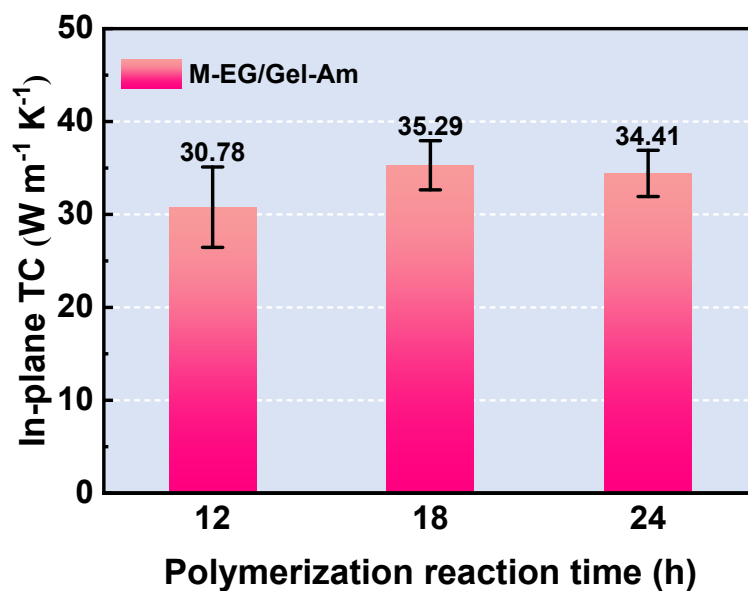


Figure S10. In-plane TC of the obtained TIMs with different polymerization reaction time.

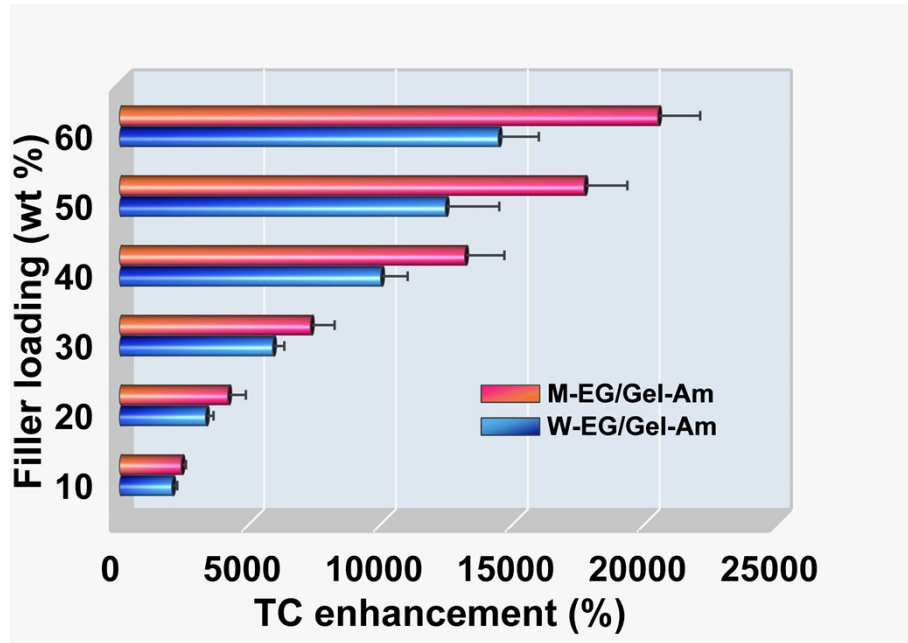


Figure S11. Specific TCE value along the in-plane direction of W-EG/Gel-Am and M-EG/Gel-Am composite.

Table S1. Comparison of the flexible polymer-based TIMs

Fillers	Fraction	Matrix	TC ($\text{W m}^{-1} \text{K}^{-1}$)	TCE (%)	Technical process	Year ^{Reference}
M-EG	42.2 vol%	Gelatin	35.29 (//*)	340.4	Normal	This work
GO	38.5 vol%	NR	20.84 (//*)	176.8	Hard	2019 ^[1]
BNNS	83 wt%	PVA	67.6 (//*)	354.6	Normal	2021 ^[2]
BNNS-OH	50 wt%	Cellulose	20.41 (//*)	155.0	Normal	2021 ^[3]
FBN	10 vol%	PAI	45.7 (//*)	100.8	Easy	2022 ^[4]
NF-BNNSs	89 wt%	PVA	6.90 (//*)	31.2	Easy	2015 ^[5]
BN	11.9 vol%	PDMS	1.58 (//*)	25.3	Easy	2020 ^[6]
BNNSs	16 wt%	PDMS	11.05 (//*)	322.6	Hard	2019 ^[7]
3DSG	11 wt%	PAI	2.63 (//*)	81.5	Hard	2015 ^[8]
rGO@CN	10 wt%	PAI	6.08 (//*)	279.5	Normal	2021 ^[9]
BNNSs	16 wt%	PDMS	11.05 (//*)	322.6	Hard	2019 ^[7]
BNNS	50 wt%	PAA	3.20 (//*)	15.1	Hard	2017 ^[10]
BNNS	30 wt%	ANF	46.7 (//*)	704.2	Hard	2020 ^[11]

Notes: BNNS: boron nitride nanosheets; FBN: functionalized boron nitride nanosheets; NR: natural rubber; 3DSG: silicon carbide (SiC) nanowires with graphene sheets; rGO@CN: reduced graphene oxide with carbon nitride; PAI: polyamide-imide; NF-BNNSs: noncovalent functionalized boron nitride

nanosheets; PAA: polyacrylic acid; ANF: aramid nanofiber. (*//*): in-plane thermal conductivity, (*⊥*): through-plane thermal conductivity. (*): LFA method.

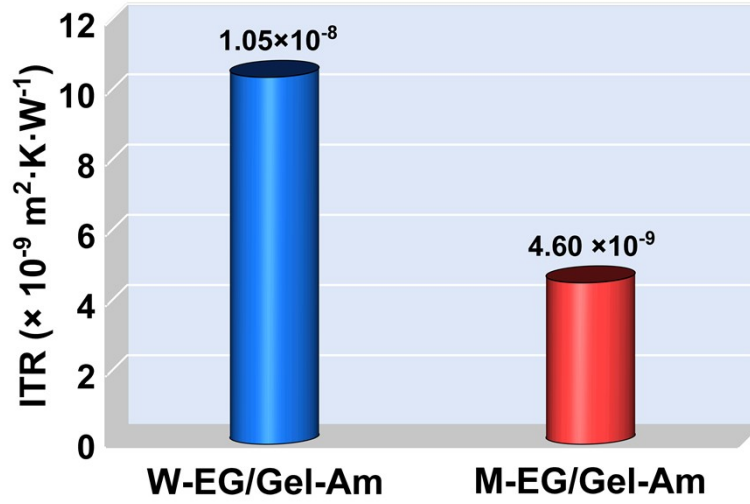


Figure S12. Calculated interfacial thermal resistance values of W-EG/Gel-Am and M-EG/Gel-Am composites.

Overlap area of fillers used in the ITR Analysis for W(P)-EG/LNBR Composites

$$S = \frac{2d^2}{\pi} \sigma(p) \quad (1)$$

$$\sigma(p) = \ln \left[\frac{\sqrt{1+p^{-1}} + \sqrt{1-p^{-1}}}{\sqrt{1+p^{-1}} - \sqrt{1-p^{-1}}} \right] \quad (2)$$

Where p is the aspect ratio (L/d) of the graphite sheet.

Table S2. Values of the relevant parameters obtained from the simulation

	K_0	V_c	t_a	R_c	R
W-EG/Gel-Am	33.26	0.253	0.205	9875.1	1.05 × 10 ⁻⁸
M-EG/Gel-Am	52.57	0.230	0.289	1906.4	4.60 × 10 ⁻⁹

```

00 tracked_robot_platform | Arduino 1.8.5
文件 编辑 项目 工具 帮助
tracked_robot_platform
#include <Stepper.h>
int ch1 = 8, ch2 = 9, relay2 = 10, ch4 = 11, ch5 = 12, ch6 = 13, relay = 13;
int ena = 5, enb = 6, in1 = 2, in2 = 3, in3 = 4, in4 = 7;
int b1 = 0, b2 = 0, b3 = 0, b4 = 0, b5 = 0, b6 = 0, b7 = 0, b8 = 0, b9 = 0, b10 = 0, delta = 0;
Stepper myStepper(80, 14, 15, 16, 17);

void setup() {
  // put your setup code here, to run once:
  pinMode(ch1, INPUT);
  pinMode(ch2, INPUT);
  pinMode(ch3, INPUT);
  pinMode(ch4, INPUT);
  pinMode(ch5, INPUT);
  pinMode(ch6, INPUT);
  pinMode(ch7, INPUT);
  pinMode(ch8, INPUT);
  pinMode(ch9, INPUT);
  pinMode(ch10, INPUT);
  digitalWrite(ena, LOW);
  digitalWrite(enb, LOW);
  digitalWrite(in1, LOW);
  digitalWrite(in2, LOW);
  digitalWrite(in3, LOW);
  digitalWrite(in4, LOW);
  Serial.begin(9600);
  digitalWrite(relay, LOW);
  digitalWrite(relay2, LOW);
  myStepper.setSpeed(60);
  pinMode(relay, OUTPUT);
  pinMode(relay2, OUTPUT);
  pinMode(in1, OUTPUT);
  pinMode(in2, OUTPUT);
  pinMode(in3, OUTPUT);
  pinMode(in4, OUTPUT);
}

void loop() {
  // put your main code here, to run repeatedly:
  b1 = pulseIn(ch1, digitalRead(ch1) == HIGH ? LOW : HIGH);
  Serial.print("ch1=");
  Serial.println(b1);
}

```

正在启动

ARDUINO Genuino

AN OPEN PROJECT WRITTEN, DEBUGGED, AND SUPPORTED BY ARDUINO.CC AND THE ARDUINO COMMUNITY WORLDWIDE

LEARN MORE ABOUT THE CONTRIBUTORS OF ARDUINO.CC on arduino.cc/credits

Arduino/Genuino Uno © COM4

Figure S13. The core code of the tracked robot platform and compiling environment.

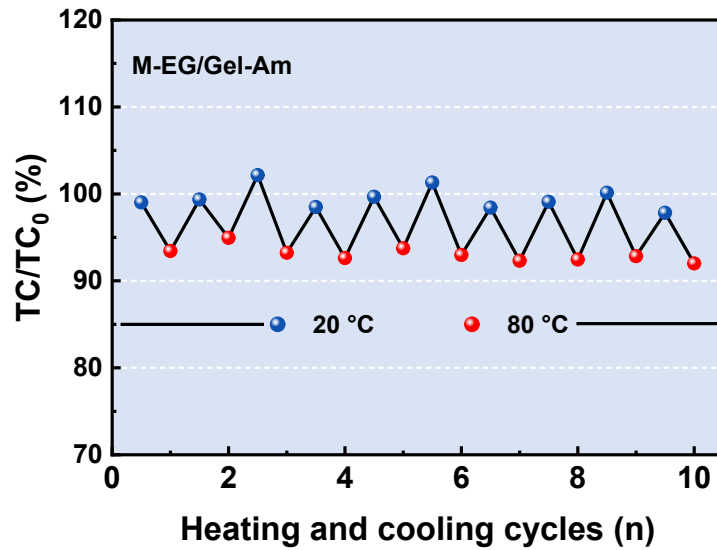


Figure S14. The variation of the in-plane thermal conductivity as a function of heating and cooling cycles.

Table S3. Values of the relevant parameters used for the simulation

	Materials	Size (cm ³)	K (W m ⁻¹ K ⁻¹)	C_p (J g K ⁻¹)
RF substrate	Copper	$3.0 \times 2.0 \times 0.3$	300	0.37
Heat sink	Alumina	$4 \times 4 \times 1.2$	40	0.90

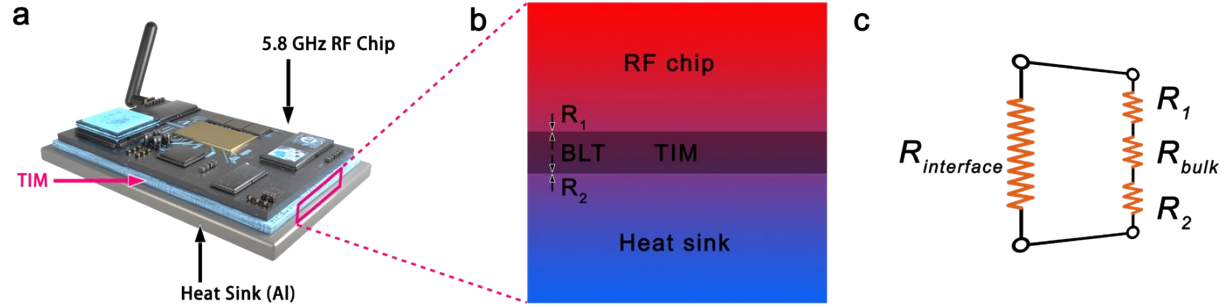


Figure S15. (a) Schematic illustration of the TIM evaluation system for mobile transmission module. (b) Magnified profile of the selected area showing the packaging structure. (c) The theoretical model used for the calculation of the thermal contact resistance of TIMs.

The thermal contact resistance (R_c) of different applied TIMs with the same bond line thickness (BLT) was calculated by the theoretical model exhibited in the **Figure S16**. The detailed parameters used in the calculation was summarized in the **Table S4**, and the thermal contact resistance can be expressed by the equation:

$$R_c = R_1 + R_2 = R_{interface} - R_{bulk} = \frac{BLT}{\kappa_{eff}} - \frac{BLT}{\kappa_{bulk}} \quad (4)$$

Table S4. The detailed parameters for model calculations and the related results

Sample	BLT (μm)	κ_{bulk} (W m ⁻¹ K ⁻¹)	R_{bulk} (W mm ⁻¹ W)	κ_{eff} (W m ⁻¹ K ⁻¹)	$R_{interface}$ (W mm ⁻¹ W)	R_c (W mm ⁻¹ W)
3M 467MP	500	5.5	90.91	3.10	1.76	192.54
M-EG/Gel-Am	500	35.29	14.17	64.60	13.29	23.45

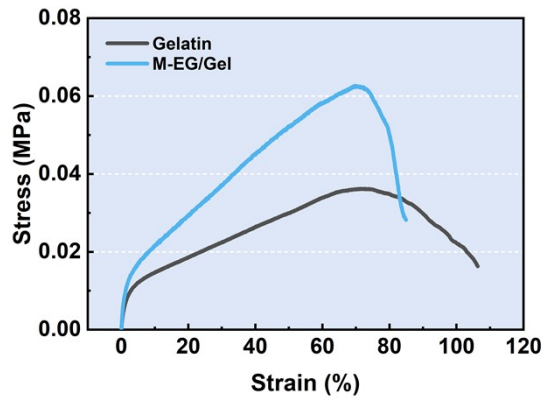


Figure. S16. Mechanical properties of the pure gelatin and M-EG/Gel composite (40 wt%).

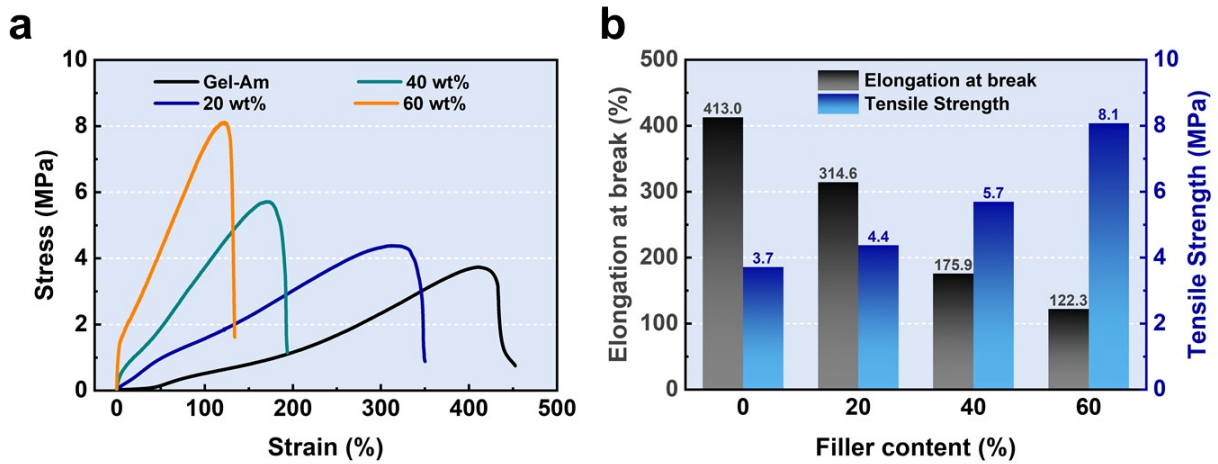


Figure. S17. Mechanical properties of the M-EG/Gel-Am composites with different filler loadings. (a) Typical stress–strain curves and (b) comparison of the elongation at break and tensile strength.

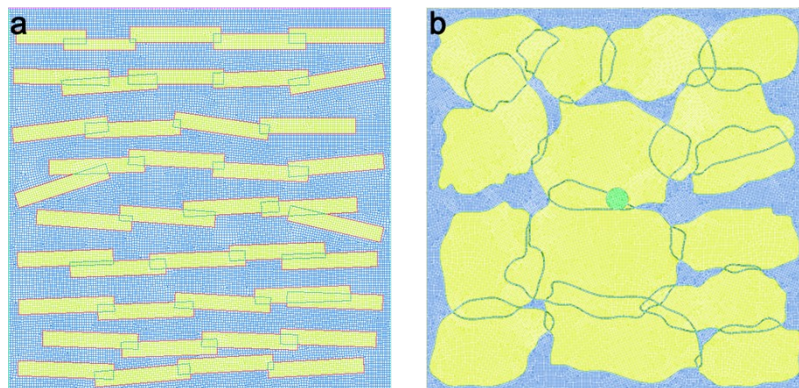


Figure S18. (a-d) The corresponding grid divisions of the LNBR matrix embedded with different microstructures along the horizontal and vertical directions, for investigation of their heat transfer capacity based on finite element simulation.

The finite element simulation based on the ANSYS was carried out to demonstrate the heat transfer capacity of the microstructure along both the horizontal and the vertical directions. In the typical configuration, a linear heat source with a fixed temperature of 80 °C was set at the bottom (left) of the simulation box to compare the heat transfer capacity along the preferred direction, the corresponding grid divisions were displayed in **Figure S18**. The background temperature was set as 20°C with a fixed convection coefficient of 10 W m⁻² K⁻¹ at all exposed surfaces.

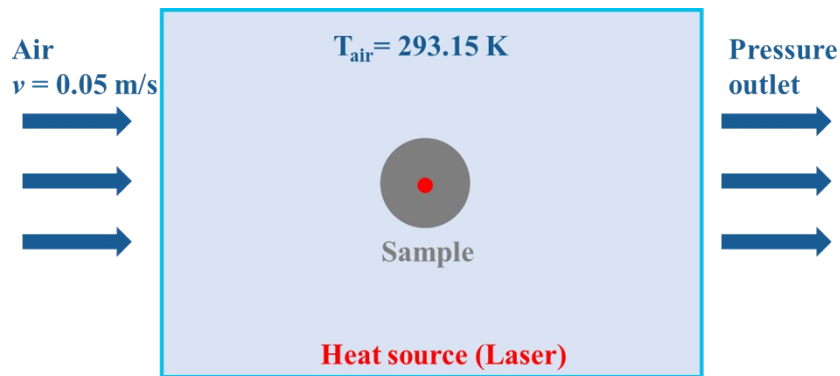


Figure S19. Boundary conditions and parameters of the simulation during heating process.

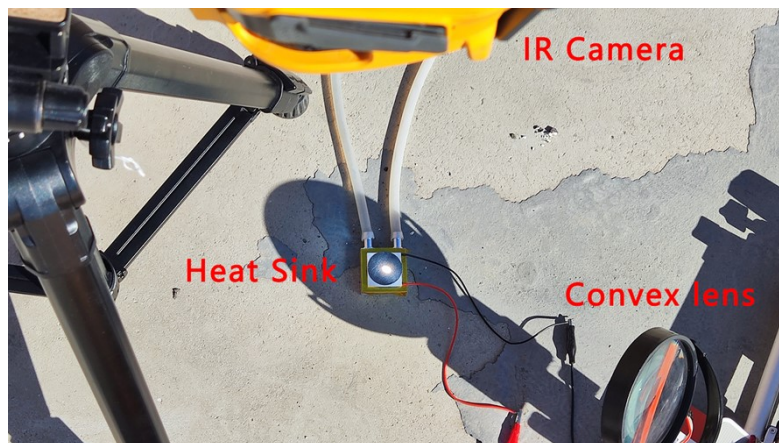


Figure S20. Optical images of self-made STEG device for solar-thermoelectric conversion.

The solar thermoelectric generator device is integrated by a convex lens, heat sink, a thermoelectric and our composite. The optical image was shown in Figure S14. Firstly, the

convex lens is set in a proper position which could concentrate the parallel sunlight onto the surface of the composite. Secondly, the accumulated solar energy was converted into thermal energy through the thermal charging process. Furthermore, the thermal energy was efficiently transferred through the composite due to the outstanding thermal conductive performance. With the modified M-EG filler in the TIM, our composite didn't need to have an extra graphite coating. Besides, the bottom of the composite was in contact with a commercial thermoelectric module (20×20 mm) which could convert thermal energy into electricity power on the basis of Seebeck effect result from the temperature difference. Finally, the output voltage and current was recorded by a multimeter, and the power density (P_{output}) was calculated by the equation $P_{\text{output}} = U^2/R$, where U and R represented the output voltage and resistance for the thermoelectric module.

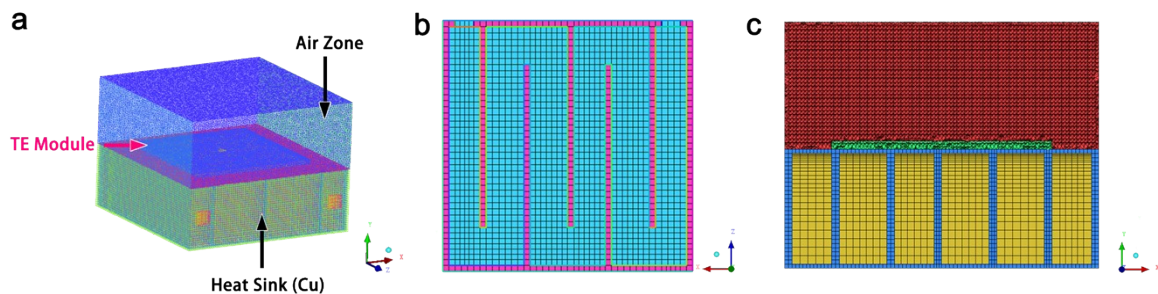


Figure S21. (a) The corresponding grid divisions of the STEG device. (b) The inner structure within the built model of the cooling water system. (c) The inner structure of the STEG device.

Table S5. Comparison in terms of output power density and energy conversion efficiency.

Sample	E_T ($W \cdot m^{-2}$)	A ($10^{-4}m^2$)	E_O ($W \cdot m^{-2}$)	η_{STEG}	Reference
GO/BN	4000	9.6	3.125	0.078	[12]
GO	2000	4.9	4.349	0.217	[13]
GO/BN	1000	4	40.28	0.210	[14]
GNPs/BN	1000	4.9	7.296	0.730	[15]
M-EG/Gel-Am	2689.2	4	165.8	1.54	This work

Notes: GO: graphene oxide; BN: boron nitride; GNPs: graphene nanoplatelets;

References

- [1] C. P. Feng, L. B. Chen, G. L. Tian, S. S. Wan, L. Bai, R. Y. Bao, Z. Y. Liu, M. B. Yang, W. Yang, *ACS Appl. Mater. Interfaces* **2019**, 11, 18739.
- [2] Q. Yan, W. Dai, J. Gao, X. Tan, L. Lv, J. Ying, X. Lu, J. Lu, Y. Yao, Q. Wei, R. Sun, J. Yu, N. Jiang, D. Chen, C. P. Wong, R. Xiang, S. Maruyama, C. T. Lin, *ACS Nano* **2021**, 15, 6489.
- [3] H. Tu, K. Xie, X. Lin, R. Zhang, F. Chen, Q. Fu, B. Duan, L. Zhang, *J. Mater. Chem. A* **2021**, 9, 10304.
- [4] S. Zhou, T. Xu, L. Jin, N. Song, P. Ding, *Compos. Sci. Technol.* **2022**, 219, 109259.
- [5] X. Zeng, L. Ye, S. Yu, H. Li, R. Sun, J. Xu, C. P. Wong, *Nanoscale* **2015**, 7, 6774.
- [6] J. Li, F. Li, X. Zhao, W. Zhang, S. Li, Y. Lu, L. Zhang, *ACS Appl. Electron. Mater.* **2020**, 2, 1661.
- [7] H. Hong, Y. H. Jung, J. S. Lee, C. Jeong, J. U. Kim, S. Lee, H. Ryu, H. Kim, Z. Ma, T. I. Kim, *Adv. Funct. Mater.* **2019**, 29, 1902575.
- [8] W. Dai, J. Yu, Y. Wang, Y. Song, F. E. Alam, K. Nishimura, C.-T. Lin, N. Jiang, *J. Mater. Chem. A* **2015**, 3, 4884.
- [9] Y. Wang, X. Zhang, X. Ding, Y. Li, P. Zhang, M. Shu, Q. Zhang, Y. Gong, K. Zheng, B. Wu, X. Tian, *Compos. Sci. Technol.* **2021**, 205, 108693.
- [10] H. Jiang, Z. Wang, H. Geng, X. Song, H. Zeng, C. Zhi, *ACS Appl. Mater. Interfaces* **2017**, 9, 10078.
- [11] K. Wu, J. Wang, D. Liu, C. Lei, D. Liu, W. Lei, Q. Fu, *Adv. Mater.* **2020**, 32, 1906939.
- [12] J. Yang, L.-S. Tang, R.-Y. Bao, L. Bai, Z.-Y. Liu, W. Yang, B.-H. Xie, M.-B. Yang, *J.*

Mater. Chem. A **2016**, *4*, 18841.

[13] R. Cao, D. Sun, L. Wang, Z. Yan, W. Liu, X. Wang, X. Zhang, *J. Mater. Chem. A* **2020**, *8*, 13207.

[14] J. Yang, L.-S. Tang, R.-Y. Bao, L. Bai, Z.-Y. Liu, W. Yang, B.-H. Xie, M.-B. Yang, *Chem. Eng. J.* **2017**, *315*, 481.

[15] D. Liu, C. Lei, K. Wu, Q. Fu, *ACS Nano* **2020**, *14*, 15738.